

# Surrogate-based Multifidelity Robust Optimization for Ducted Fan Blade Aerodynamic Design

Richard Amankwa Adjei\*  
Department of Mechanical  
Materials and Manufacturing,  
Control Systems Laboratory  
University of Nottingham Ningbo  
China  
Ningbo, China  
Richard-  
Amankwa.Adjei@nottingham.ed  
u.cn

Salman Ijaz  
Department of Mechanical  
Materials and Manufacturing,  
Control Systems Laboratory  
University of Nottingham Ningbo  
China  
Ningbo, China  
salman.ijaz@nottingham.edu.  
cn

Junyuan Jiang  
Department of Mechanical  
Materials and Manufacturing  
University of Nottingham Ningbo  
China  
Ningbo, China  
ssyjj1@nottingham.edu.cn

Yiwei Wang  
Department of Mechanical  
Materials and Manufacturing  
University of Nottingham Ningbo  
China  
Ningbo, China  
ssyyw13@nottingham.edu.cn

**Abstract**—Directly accounting for uncertainty and design variability in a multidisciplinary design process of turbomachinery blades is essential to ensure design robustness and reliability from preliminary to manufacturing design process. However, performing such an optimization task can be computationally expensive, requiring many evaluations of the numerical model to compute the statistics of the blade performance. This paper proposes and implements an efficient multifidelity approach to robust optimization that leverages the benefits of neural networks, based on high-fidelity computational fluid dynamics (CFD) datasets and multiple inexpensive low-fidelity regression models for uncertainty quantification. The multi-information source is integrated using a multifidelity Monte Carlo method that optimally allocates the computational load based on relative evaluation cost and the strength of the correlation to achieve the relevant design statistics for the target objectives. The results showed that the proposed optimization strategy achieved mean aerodynamic performance with variations of 3.26%, 16.67% and 1.98% for isentropic efficiency, total pressure ratio and pressure coefficient. Moreover, the total pressure ratio realized the highest reduction in standard deviation of 25%. By combining neural networks with cheap regression models the robust optimization solution was able to predict the statistical objective targets with reasonable accuracy.

**Keywords**—multifidelity Monte Carlo, electric ducted fan, artificial neural network, robust optimization, data mining, uncertainty quantification

## I. INTRODUCTION

In order to achieve environmentally friendly and greener aviation propulsion, disparity between manufactured and original design intent should be minimized to achieve more robust prediction of motor power to weight ratio, vehicle control and aeropropulsive performance of distributed electric propulsion systems (DEP). This is particularly useful for miniature parts such as small propulsors of DEPs that are used to enhance the acoustic shielding effect of airframes in order to reduce noise signatures [1-3]. The spatial distribution of blade

and nacelle surface deviations propagates uncertainty in rotor-stator interactions, leakage and secondary flows at design and off-design conditions. Such variations are highly stochastic and are therefore essential to account for geometric uncertainty from preliminary design of individual components to airframe-propulsor integration design [4].

The influence of ducted fan blade and endwall profiles on aerodynamic and structural performance for both large and small-scale DEP applications has been studied extensively over the years [5]. Key profile parameters such as the hub-to-tip ratio, hub cap installation distance and stagger angle particularly at mid-span and tip were found to be sensitive to fan efficiency by approximately 0.25% - 1.4%, notwithstanding the fact that the hub-to-tip ratio is generally restricted due to mechanical constraints [6]. Parametric studies by Fan et al [7] also observed a strong influence of stagger angle and sweep on the aerostuctural performance of an electric ducted fan rotor at different operating conditions. Similar studies were performed by Zhang et al [8] on the influence of rotor radius, pitch chord, stagger, and duct thickness on thrust, power, and torque. For design parameters that are sensitive to small changes, uncertainty propagation greatly reduces design robustness and service lifetime.

Robust optimization helps to realize desensitized blades shapes with optimum performance predictions compared to deterministic solutions that do not consider the impact of uncertainties on propulsor performance. Various strategies using uncertainty methods such as the Monte Carlo method [9], non-intrusive polynomial chaos [10] and active subspaces [11] have been implemented using mostly high-fidelity CFD datasets. Nonetheless, for large-scale parametric studies, existing robust optimization methods still suffer from the curse of dimensionality and is unrealistic to use high-fidelity CFD simulations for limited computation cost and time. Furthermore, the accurate prediction of the spatial variation of the blade surface distribution is limited to the type of geometric parametrization method used. The manufactured blade surface

possesses some randomness in its properties which sometimes varies significantly over the surface area [12]. For a realistic interpretation of such random deviations, a metamodel that accurately captures the spatial variation in the form of a random field is highly essential for robust optimization.

For limited computational budget, the cost of acquiring enough data to accurately construct a stochastic model for robust optimization is very challenging. Over the years, several stochastic models have been developed to accelerate the design cycle time while maintaining solution accuracy when very few observations are available. Multifidelity and multilevel methods have been shown to be effective in accelerating the design process by combining several fidelity models. It exploits low-fidelity models to reduce the runtime and computation cost, and recourse to the high-fidelity to preserve the model accuracy [13-15]. Mohammadi-Ahmar et al [16] used bi-fidelity model based on compressed sensing and polynomial chaos kriging (PCK) uncertainty of a turbine blade leading edge film cooling. Using geometric and operational uncertainties, the bi-fidelity model reduced the computation cost by 80%. Recent studies by Tao and Sun [17] developed and implemented a deep learning-based multifidelity surrogate model for robust aerodynamic optimization. For Jabarullah Khan and Elsheikh [18], a novel hybrid multifidelity multilevel Monte Carlo was proposed and applied to a two-phase flow uncertainty quantification problem. Computing times showed speedups that ranged from 8 up to 19 compared with standard Monte Carlo method with high-fidelity datasets. Other multifidelity models based on nonintrusive proper orthogonal decomposition (POD) [19] and Krylov subspaces [20] have also been implemented to generate reduced order basis approximations of high-fidelity datasets.

In this paper, a robust design optimization framework that integrates neural networks for multifidelity uncertainty analysis is presented. The main focus of this work is to directly implement uncertainty in the design and optimization process by means of a multifidelity Monte Carlo method while maintaining modeling accuracy. The neural network integrated multifidelity model combines high-fidelity CFD datasets and cheap low-fidelity regression models for dimensionality reduction and accelerated design process. The paper is organized as follows; a brief description of the baseline electric ducted fan and numerical model validation is presented. This is followed by parametric modeling and definition of geometric deviations. The multifidelity approach for UQ and robust optimization is subsequently presented, and the obtained results are discussed. Finally, some conclusions and future prospects are given.

## II. BASELINE DESIGN

The baseline design is an electric ducted fan (EDF) propulsor with 10 blades designed for distributed electric propulsion system. It has an outer diameter of 120mm and a hub-to-tip ratio of 0.33[21]. It is part of a series of experimental designs for ducted fan noise reduction research. The blades are made of high-grade aluminum alloy in order to obtain a rigid structure with relatively low weight. The fan rotor is powered by a 5060 750KV motor using a 44.4 V Lithium polymer battery (12S LiPo battery). The target task of the electric ducted fan was to produce a power and thrust of about 5000W and 70N respectively. Fig.1 and Table 1 show the airfoil profiles from

hub to tip and design specifications of the axial flow fan respectively.

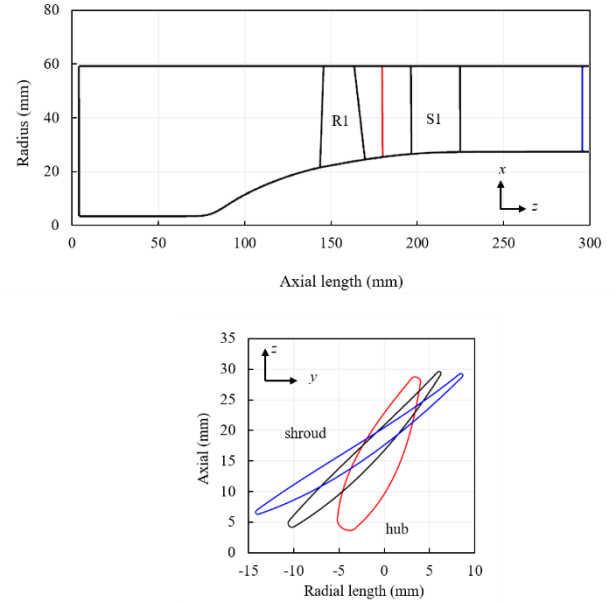


Fig.1 Schematic of aerodynamic flow path for the ducted fan propulsor.

TABLE.I PERFORMANCE SPECIFICATIONS FOR THE EDF PROPULSOR.

Parameters	value	units
Hub diameter, $D_h$	30	mm
Tip diameter, $D_{sh}$	120	mm
Tip clearance, $\tau$	0.5	mm
Rotor Speed, $\Omega$	50000	rpm
R1/S2 count	10/22	-
Efficiency, $\eta$	84.6	%
Pressure ratio, $\pi$	1.19	-

### A. Numerical Validation

Numerical computations performed for the electric ducted fan propulsor were undertaken using the steady-state Reynolds averaged Navier–Stokes solver, ANSYS CFX (19.2) [22]. The single passage setup consisted of two single passage stators, and an unshrouded rotor with counter-rotating casing boundary condition. The shear stress transport model ( $k - \omega$  SST) was employed for turbulence closure. Considering the estimated high Reynolds number, a full turbulence condition was selected with high resolution advection scheme and first order discretization. For the steady-state run, the so-called mixing-plane between rotating and non-rotating blade rows, which mixes out circumferential variations of the flow velocities and pressures, was chosen to simulate the rotor-stator interaction. The H-type grid for block meshing was used to generate a total of 2.5 million mesh elements using ANSYS TurboGrid [23]. Fig.2 illustrates the computational domain and the block mesh elements used in this study. Similar grid sensitivity study and finite element analysis (FEM) were computed using the multiphysics commercial solver ANSYS Mechanical (19.2) [24] for the rotor blade structural analysis. The material properties of the Aluminum alloy used are given in Table 2. The blade root had a fillet with a radius of 1.5 mm. The predetermined threshold

mesh used to compute the total, radial deformation and static stress was about 626617 elements. The FEM analysis was accounted for considering only the centrifugal force due to rotation since it's the most dominant force on static stress and radial deformation of the rotor blade.

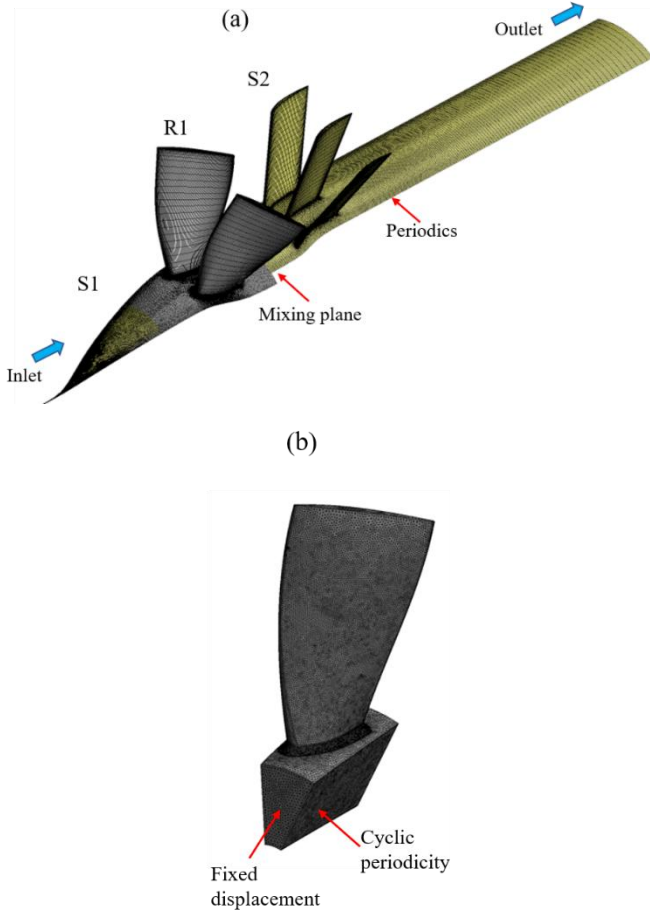


Fig.2 CFD grid nodes distribution for the electric ducted fan.

TABLE.II MATERIAL PROPERTIES FOR ALUMINUM ALLOY

Property	Value	Unit
Density	2770	kg/m3
Young's modulus	71	Gpa
Tensile yield strength	280	Mpa
Poisson ratio	0.3	

In addition, since the information of the true function for uncertainty quantification study isn't known a priori, it is imperative to estimate the discretization error to ensure that the uncertainty in the CFD simulation has minimal influence on the true solution as predicted. This is to ensure that the assumption that the high-fidelity surrogate model is the true function of the CFD simulations can be said to be valid. The procedure adopted for estimating the discretization error follows that of the Richardson extrapolation method [25]. Since the grid level and the flux limiter both determine the spatial resolution and accuracy of the numerical solution, the magnitude of the

discretization error for the set of grids showing monotonic convergence is estimated. This is to ensure that the selected grid size is above the threshold limit with minimal error margin. For each grid case, fully turbulent closure was simulated for the fan stage efficiency ( $\eta$ ) and total pressure ratio ( $\pi$ ). The discretization error at a grid level,  $k$ , is calculated as

$$\phi_{\text{error}}(\%) = \left| \frac{\tilde{n}_{\text{eff},k} - \tilde{n}_{\text{eff},\text{exact}}}{\tilde{n}_{\text{eff},\text{exact}}} \times 100 \right| \quad (1)$$

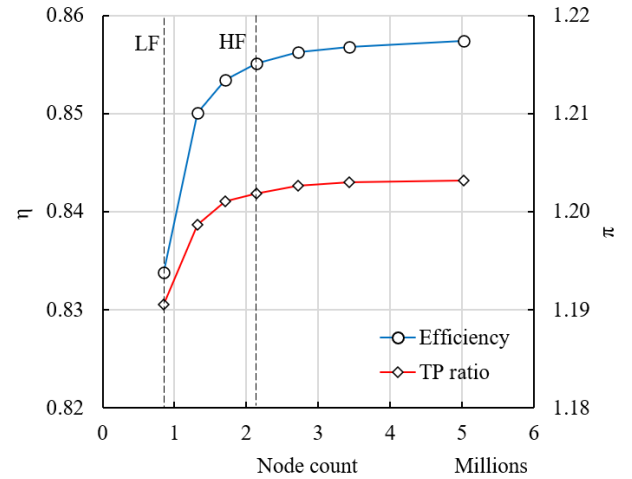
Where  $\tilde{n}_{\text{eff},k}$  and  $\tilde{n}_{\text{eff},\text{exact}}$  are the computed efficiency values at grid level  $k$  and the approximation to the exact value of  $\tilde{n}_{\text{eff}}$  respectively. The approximate value of the observed numerical order accuracy,  $\tilde{p}$ , and the  $\tilde{n}_{\text{eff},\text{exact}}$  are computed from three grid levels, M3, M4, and M5 as:

$$\tilde{p} = \frac{\ln\left(\frac{\varepsilon_{75}}{\varepsilon_{53}}\right)}{\ln(r)} \quad (2)$$

$$\tilde{n}_{\text{eff},\text{exact}} = \tilde{n}_{\text{eff},5} - \frac{\varepsilon_{53}}{r^{\tilde{p}-1}} \quad (3)$$

Where  $r$  is the ratio of grid spacing,  $\varepsilon_{53}$  and  $\varepsilon_{75}$ , the difference between the solutions of grid levels 3-5 and 5-7. Furthermore,  $r^{\tilde{p}} = (\varepsilon_{53} + \varepsilon_{75}/\varepsilon_{53}) - 1$ .

Table 3 and Fig. 3 show the  $\tilde{p}$  value and solutions for the different grid levels and plots of the absolute value for the discretization error (%) against  $h$  values respectively. From the estimated discretization error for isentropic efficiency, M3 to M5 have errors of 1.019% and 0.696% which are lower than 2%. This can be said to be reasonable with minimal effect on the CFD solution. M1 and M2, on the other hand, had values significantly greater than 1%. Total pressure ratio results also showed a similar trend much lower in magnitude. Hence, for the multifidelity modeling, mesh size greater than M3 was used to compute the dataset for the high-fidelity modeling and M1, for the low-fidelity dataset.



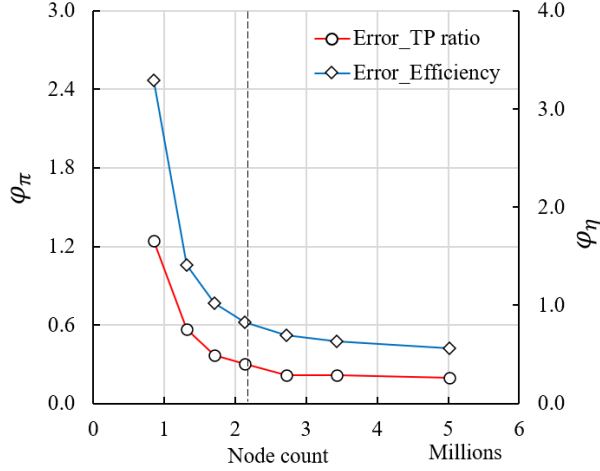


Fig.3 Grid independence study and discretization error estimation for various grid sizes.

TABLE.III ESTIMATION OF DISCRETIZATION ERROR

Grid size	Stage	$\varphi_\eta(\%)$	$\varphi_\pi(\%)$	$\tilde{p}$ value ( $\eta$ )	$\tilde{p}$ value ( $\pi$ )
M3	1704528	1.019	0.371	1.407	1.766
M5	2724822	0.696	0.214		
M7	5022384	0.560	0.197		

To further enhance computational credibility, a similar strategy is applied to the baseline CFD setup and the associated flow features were further checked using the NASA Rotor 67 [26, 27]. Similar boundary conditions of total pressure and temperature at the inlet and mass flow rate were imposed with frozen rotor interface type. The running tip clearance defined was 0.61mm, rotating at a speed of 16043 rpm. The mesh element size used was 1545200 elements. At design point, the total pressure ratio is 1.63 at a mass flow rate of 33.25 kg/s.

Fig. 4a and 4b shows a comparison of aerodynamic performance map of NASA Rotor 67. The CFD results were in good agreement with the experiment. Total pressure ratio predicts well at near choke but marginally under predicted at near peak efficiency and surge. On the contrary, adiabatic efficiency marginally over predicted at near surge. The observed trend is analogous to the results of Liou et al [28] and Chima [29]. From Fig.4b, contour plots of Mach number at 30% and 70% from shroud showed good prediction of the bow shock and its interaction with the boundary layer at the blade suction surface. The Mach number magnitudes and distribution at the LE was also well predicted value of about 1.5 for 30% span but overpredicted for 70% compared to the experiments. Further downstream of the rotor blade, the Mach number magnitudes and distribution showed good prediction ranging from 0.7- 0.8 at 70% and 0.8 to 1 at 30% spanwise length. Altogether, the CFD results were in reasonable agreement with experiments published in the open literature although there were some

differences. The computational model implemented can, consequently, be said to be valid for our studies.

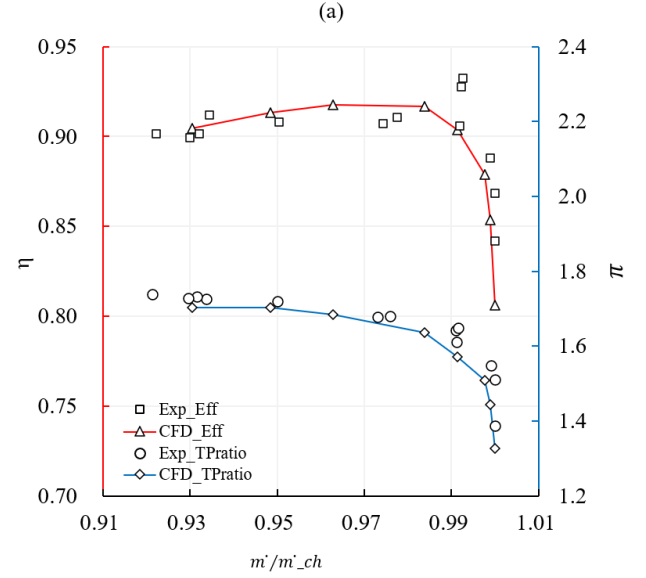


Fig.4 Aerodynamic performance of NASA Rotor 67.

### B. Performance and Stress Analysis

Figs. 5, 6 and 7 show the aerodynamic performance, flow field and pressure distribution on the rotor and stator blades. It's worth mentioning that, since the blade operates with high tip Mach number for the given rotating speed, effect of fluid compressibility was considered. Air was defined as an ideal gas rather than a gas with constant density. The performance map follows the trend of a typical axial flow fan. The isentropic efficiency at high flow rates (choke) was relatively higher than the efficiency at low flow rates (near surge). At choke flow, high Mach number flow along with strong passage shock was observed at the mid-section of the blade SS and LE area of the blade PS. The streamline distribution as shown in Fig. 6, predicts LE separation and a massive endwall separation from the mid-section of the hub profile and moves downstream to the TE at about 0.75 spanwise length. Moreover, the interaction of the passage shock with the boundary layer also caused flow separation from blade tip down to about 0.85 spanwise length. Towards peak efficiency, the LE separation became more evident and extended towards the blade tip. The endwall and shock-boundary layer interaction pushed much further to the mid-section of the blade profile from hub to shroud. This is evident in Fig.7 where there is a sharp drop in pressure at about 0.5 chordwise for 0.9 span compared to 0.5 span on rotor blade. The onset of flow instability is evident at low flow rate below 1.35 kg/s, where there is a sharp drop in total pressure ratio. Towards surge, there is a gradual increase in the total pressure ratio with an abrupt decrease in isentropic efficiency. Streamline distribution shows an even more pronounced separation at the blade LE and the shock separation shifts further towards the LE. For the FEM analysis, Fig.8 shows the von-mises stress at the PS side and the root of the blade at a rotating speed of 50000 rpm. The fan blade static stress was mainly highest at the LE root of the blade PS and its magnitude was well below the yield stress of the material. The radial displacement of the blade (not

shown here) was about 0.045mm, which is 0.23 units of tip clearance, TC. The radial displacement of the blade can therefore be said to be in the tolerable gap without causing the blade to rub the casing. For the robust optimization study, only the blade static stress was considered as an objective to assess its correlation with aerodynamic performance.

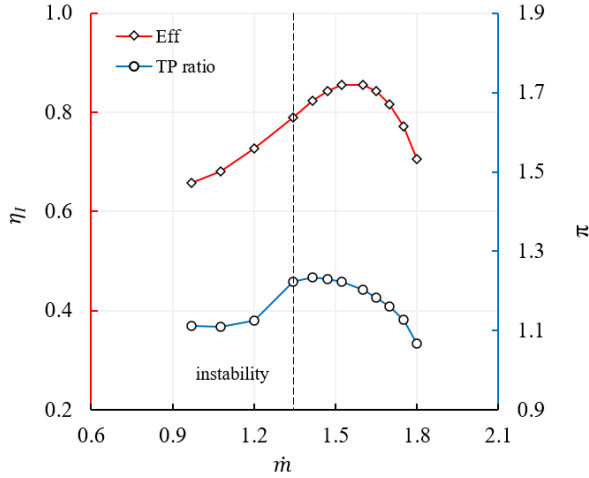


Fig.5 Aerodynamic performance for the ducted fan propulsor.

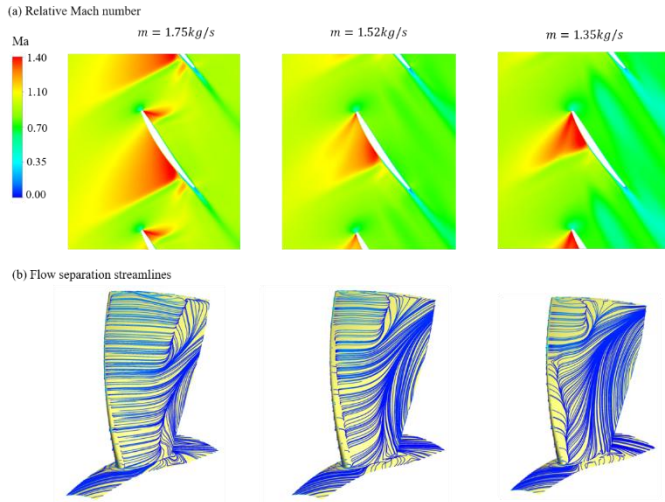


Fig.6 Flow field and streamline distribution on fan rotor and stator at mass flow  $m = 1.6 \text{ kg/s}$

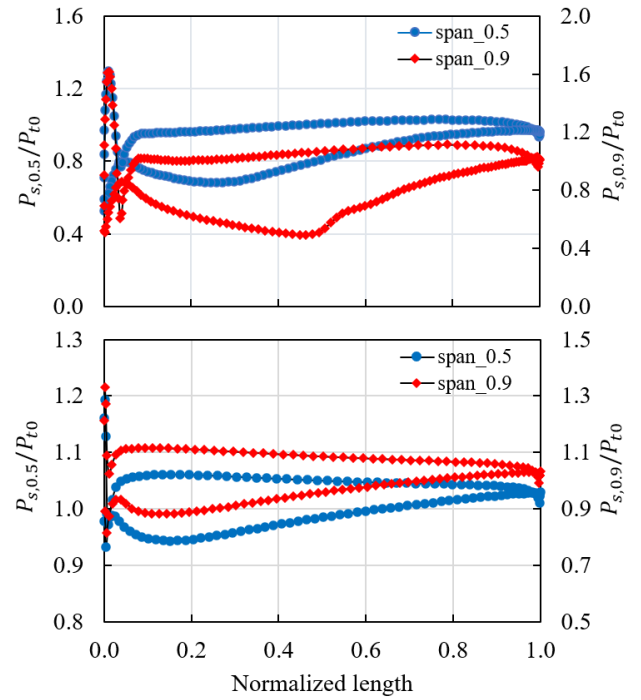


Fig.7 Blade pressure distribution of fan rotor at mass flow  $m = 1.52 \text{ kg/s}$

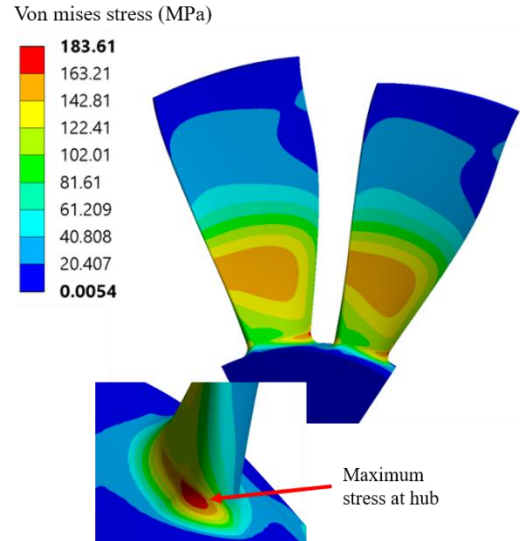


Fig.8 Static stress distribution and FEM regression of fan wheel.

### III. ROBUST OPTIMIZATION STRATEGY

#### A. Blade Parameterization

The baseline EDF fan stage was parameterized using b-spline curves and NURBS metasurface method. A generic 2D profile curve was generated using a feature code from hub to shroud for each blade. A predefined stacking axis was used to define the blade profiles in 3D and a NURBS metasurface was used to generate the three-dimensional blade using function curves [30]. The function curves were used to define the conventional design variables. The exact blade geometry data was subsequently used to adjust and capture the 3D shape of the rotor and stator blades.



Blade parametrization was for key design parameters such as LE and TE radiuses, camber, chord, thickness distribution, lean, sweep, blade metal angles and tip clearance were defined for the rotor blade. Similar parameters were also described for the stator blade. The stagger angle was kept constant. Four B-spline control points were defined for each function curve. For the rotor, since a fillet was specified at the blade root, parameters near the roots were considered non-influential and were therefore kept constant. A total of 12 design variables were defined for the stator and 25 for the rotor blade. Table 4 shows a total of 37 design variables defined for both the rotor and stator blades.

TABLE.IV ENGINEERING DESIGN PARAMETERS

Stage parameters	Function curve	Count
LE metal angle	b-spline curve	5
TE metal angle		5
LE radius	b-spline curve	5
TE radius		5
LE SS/PS thickness	b-spline curve	6
TE SS/PS thickness		3
Lean factor	b-spline curve	2
Sweep factor		2
Chord	b-spline curve	3
Tip clearance	Point control	1
Total		37

### B. Multifidelity Uncertainty Quantification

A surrogate-based multifidelity Monte Carlo (MFMC) approach, introduced by Peherstorfer et al [31], was used to was used as the reference method to quantify and optimize the geometric uncertainty existing within the design of the electric ducted fan. To achieve a multifidelity stochastic model, high and low-fidelity models were combined using control variate method as derivatives of the multifidelity estimator. Evaluations between each model fidelity were balanced for every run time such that, the mean square error (MSE) of the estimator was minimized for a given computational budget  $p$ . The MFMC estimator is given as:

$$\hat{s} = \bar{y}_{m1}^{(1)} + \sum_{i=2}^k \alpha_i (\bar{y}_{mi}^{(i)} - \bar{y}_{mi-1}^{(i)}) \quad (4)$$

Where  $\alpha_2, \dots, \dots, \alpha_k \in$  are coefficients that weight the differences  $\bar{y}_{mi}^{(i)} - \bar{y}_{mi-1}^{(i)}$  of the Monte Carlo estimates  $\bar{y}_{m1}^{(1)}$  and  $\bar{y}_{mi-1}^{(i)}$  for  $i = 2, \dots, k$ . The MSE of  $\hat{s}$  with respect to  $s$  is derived as:

TABLE.V MSE ERROR VALUES FOR HIGH-FIDELITY AND LOW-FIDELITY MODELS

Fidelity	Model	Sample	MSE	$R^2$
HF	ANN	171	1.18E-05	0.991
LF	NL	171	1.83E-05	0.986
	PLS	171	2.62E-05	0.969
	ANOVA	171	2.26E-05	0.977

$$e(\hat{s}) = E[(s - \hat{s})^2] = \text{Vars}[\hat{s}] \quad (5)$$

And the cost of estimating the MFMC,  $\hat{s}$ , is derived as:

$$c(\hat{s}) = \sum_{i=1}^k w_i m_i = w^T m \quad (6)$$

To select the optimal number of model evaluations of  $m$  and of the coefficients for a given set of high and low-fidelity surrogate models, an inner optimization loop was used. The optimization problem was formulated by minimizing the variance  $\text{Vars}[\hat{s}]$  of the MFMC estimator considering  $m \in k$  at a cost equal to the computational budget  $p$ . Further details of the MFMC theorem, PDE numerical experiments and applications can be found in Refs [32, 33].

For this research work, four sets of high and low-fidelity models were used to estimate the mean and standard deviation or variance of the objective functions. Generally, for a given number of design variables, say  $X \in$ , the number of cases for DoE needed to sufficiently search the design space should be at least 10 times (10X) the size of the design variables. For large number of variables, or multidisciplinary multicomponent problem, large number of DoE samples are needed. Furthermore, uncertainty propagation also requires an even larger amount of data which is practically impossible due to the computational cost. Machine learning models such as ANN or DNN can be suitable alternatives for constructing high-fidelity models with limited datasets. Fig. 9 shows a comparison of regression plots for ANN and PCE surrogate models. It is evident that, for limited data of 171 samples (about 4.62 times the size of the design variables), ANN predicts more accurately with an  $R^2$  value of 0.991 compared with PCE with a value of 0.940. This implies that machine learning models are advantageous in maintaining the accuracy for limited dataset.

To assess the computational cost for the multifidelity model, different combinations of high and low-fidelity models were computed to select the best with the lowest MSE error.

High-fidelity model ( $f^{(1)}$ ) - Fine mesh CFD surrogate model using artificial neural network (ANN). It uses the Bayesian regularization training algorithm which is a good generalization approach for difficult, small, or noisy datasets. 171 cases were used for training and 100 cases for testing the model.

- Low-fidelity model ( $f^{(2)}$ ) – The nonlinear regression model (NLR) obtained from the high-fidelity datasets.
- Low-fidelity model ( $f^{(3)}$ ) – The partial least squares regression model (PLS) obtained from the high-fidelity datasets.

Low-fidelity model ( $f^{(4)}$ ) – The analysis of variance regression model (ANOVA) obtained from the high-fidelity datasets.

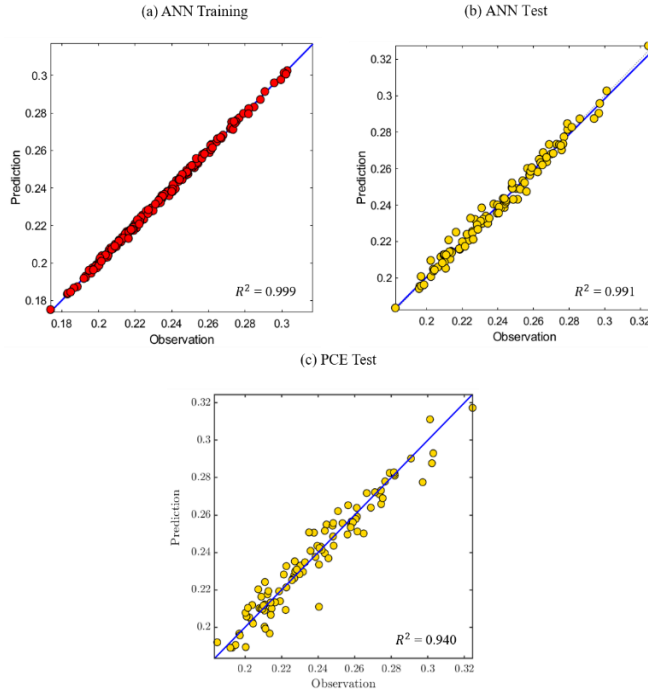


Fig. 9 Regression plots for isentropic efficiency, total pressure ratio and static stress.

The regression models were constructed using the open-source code UQlab [34], whereas ANN was programmed in MATLAB. Fig. 10 shows a comparison of the mean square error (MSE) estimate for HFMC and MFMC of isentropic efficiency, total pressure ratio and static stress. Considering a given estimated MSE error of  $1e-7$ , the computation budget decreased by about 10 times for the MFMC of both efficiency and pressure ratio compared with HF only respectively. Cp showed the least reduction of about 2 times the size of standard MC. A combination of all objectives showed significant reduction in computational budget for MFMC compared with MC. Furthermore, studies on the effect of HF sample size (not shown here) considering 50, 100, and 150 samples showed that the accuracy of the MFMC, especially the standard deviation, was strongly influenced by the sample size. Similar observations were drawn by Giselle Fernández-Godino et al [35]. It was advised that when the number of HF simulations is severely limited, there is an advantage of using the LF simulations for identifying the most important variables and it often avoids a substantial loss of solution accuracy. It can be inferred that a sensitivity-based approach to multifidelity modeling can help prevent loss of solution accuracy. Extensive investigations are needed since this may vary from one problem to another.

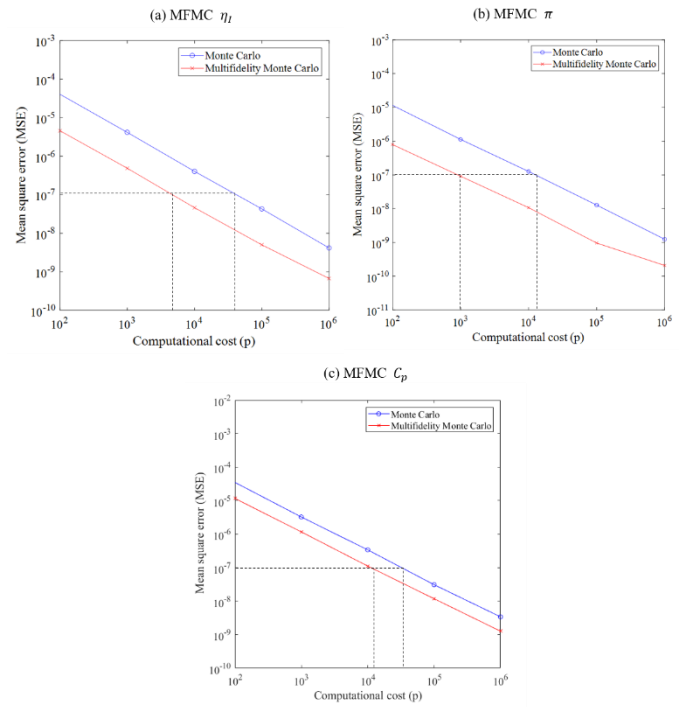


Fig. 10 Plot of mean squared error and computational budget for Monte Carlo solution and multifidelity Monte Carlo.

### C. Optimization Objectives and Constraints

The robust optimization was run using the Multi-objective Genetic Algorithm (MOGA) embedded in DAKOA optimization tool [36], as shown in the process flow chart in Fig. 11. In order to achieve an automated routine, tight coupling of the CFD tools by means of scripting was used for parsing, and evaluating surrogate models using arbitrary ASCII input, MATLAB scripts and output text files. The scripts were run in a closed automated loop via a batch file. The design variables used for the robust design were the most influential variables observed from the sensitivity study. The optimum robust design was searched within the mean and standard deviation of the initial lower and upper bound definition and tolerance band as shown in Table 6.

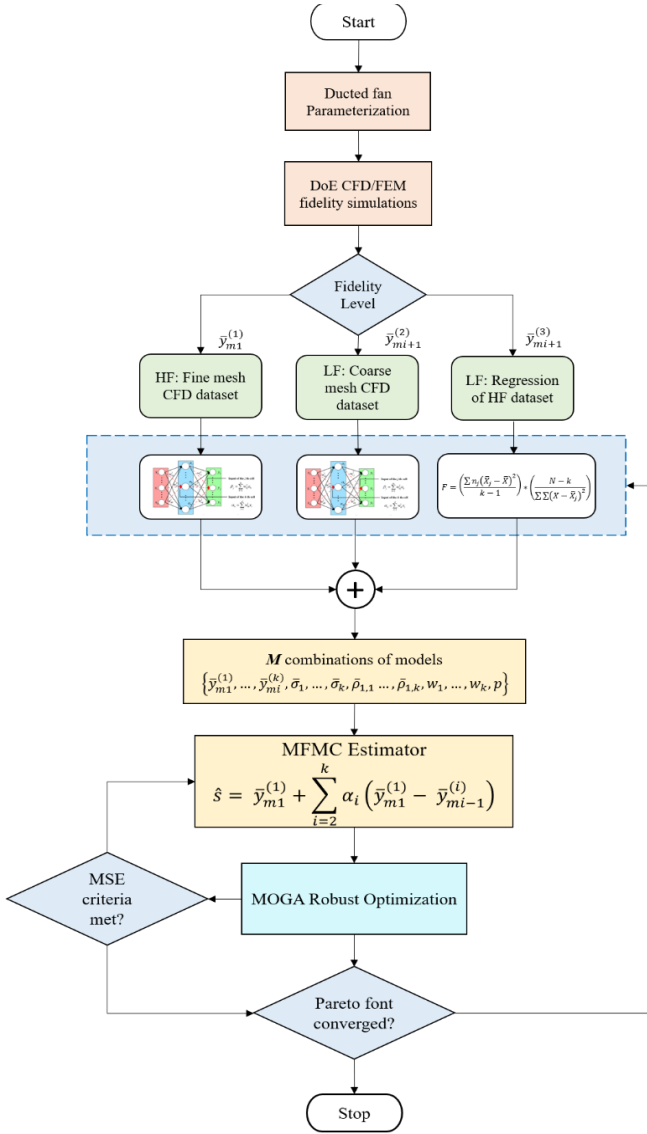


Fig.11 Process flowchart for the multifidelity optimization considering geometric uncertainty.

TABLE VI TOLERANCE SPECIFICATIONS FOR UNCERTAINTY QUANTIFICATION

Deviations for nominal size range (mm)	Tolerance class	
<i>Linear dimensions</i>	<i>Medium</i>	<i>Fine</i>
0.5 - 3	±0.10	±0.05
3 - 6	±0.10	±0.05
6 - 30	±0.20	±0.10
30 - 120	±0.30	±0.15
120 - 400	±0.50	±0.20
<i>Angular dimensions</i>		
Up to 10	±1°	±1°
10 - 50	±0.5°	±0.5°
50 - 120	±0.33°	±0.33°

#### D. Optimization Objectives and Uncertainty

Three key objectives considered were the electric ducted fan stage isentropic efficiency ( $\eta$ ) and total pressure ratio ( $\pi$ ) and

$\xi$  value. Static stress ( $\sigma_{stress}$ ) was considered a constraint. Hence, a multi-objective robust optimization problem and the objective functions are defined as:

Minimize:  $y = f(x)$

$$\Delta\eta = \frac{1-\eta_i}{\eta_{base}} \quad (7)$$

$$\Delta\pi = \frac{1.22-\pi_i}{\pi_{base}} \quad (8)$$

Subject to:  $g(x) \leq 0, h(x) \leq 0$

$$\sigma_i \leq \sigma_{s,surf} \quad (9)$$

$$\sigma_i \leq \sigma_{s,max} \quad (10)$$

$$\alpha_{r1} \leq \alpha_{r1} \leq \alpha_{r2} \quad (11)$$

$$\alpha_{s1} \leq \alpha_{s1} \leq \alpha_{s2} \quad (12)$$

The boundary conditions for manufacturing uncertainty were defined based on the ISO general tolerance standards for linear and angular dimensions [37]. The medium tolerance class designation was used to define permissible deviations considering uniform probability distribution. The mean and the standard deviations of the objectives were combined into a single performance mean ( $F_{mean}$ ) and deviation ( $F_{std}$ ) functions as represented in Eqns. (13) and (14) as:

$$F_{mean} = \left[ \frac{\mu_\eta}{\mu_{\eta 0}} + \frac{\mu_\pi}{\mu_{\pi 0}} + \frac{\mu_\xi}{\mu_{\xi 0}} \right] \quad (13)$$

$$F_{std} = \left[ \frac{\sigma_\eta}{\sigma_{\eta 0}} + \frac{\sigma_\pi}{\sigma_{\pi 0}} + \frac{\sigma_\xi}{\sigma_{\xi 0}} \right] \quad (14)$$

#### IV. RESULTS AND CALCULATION

In this section, the flow mechanisms responsible for the observed performance improvements are discussed. First and foremost, sensitivity study of the key geometrical changes for the robust design are discussed to highlight their distinct features compared with the baseline design. For simplicity, baseline and robust designs are denoted as BS and RS respectively and will be used as such in subsequent sections. Likewise, performance for the two designs is compared at  $\dot{m} = 1.6 \text{ kg/s}$  as indicated in Fig.18.

##### A. Sensitivity Study and Data Mining

In order to identify and understand the existing patterns and relationship between design variables and objective functions, it's important to establish a correlation between them. Fig.12 shows sensitivity bar chart for efficiency and pressure ratio. The sensitivity is expressed in terms of standardized regression coefficients with 95% confidence interval. A positive correlation shows positive standardized coefficient and vice versa. Furthermore, the strength or magnitude of the coefficient indicates the variables influence on the objective function. For  $\eta_I$ , two stator design variables, namely, camber tangent at the LE hub and shroud, showed significant influence with a positive correlation. Thickness distribution at the mid-section, and the camber tangent at the TE hub and shroud also showed positive correlation with moderate influence. For the rotor, the magnitude of radius at LE and TE, thickness at LE and TE, and tip clearance was significant with positive correlation. Other



parameters such as sweep factor and blade chord length showed negative correlation. Similar trend was also observed for  $\pi$  objective. However, stator design variables had relatively minimal effect compared to that of the rotor. Tip clearance and TE thickness distribution showed significant influence.

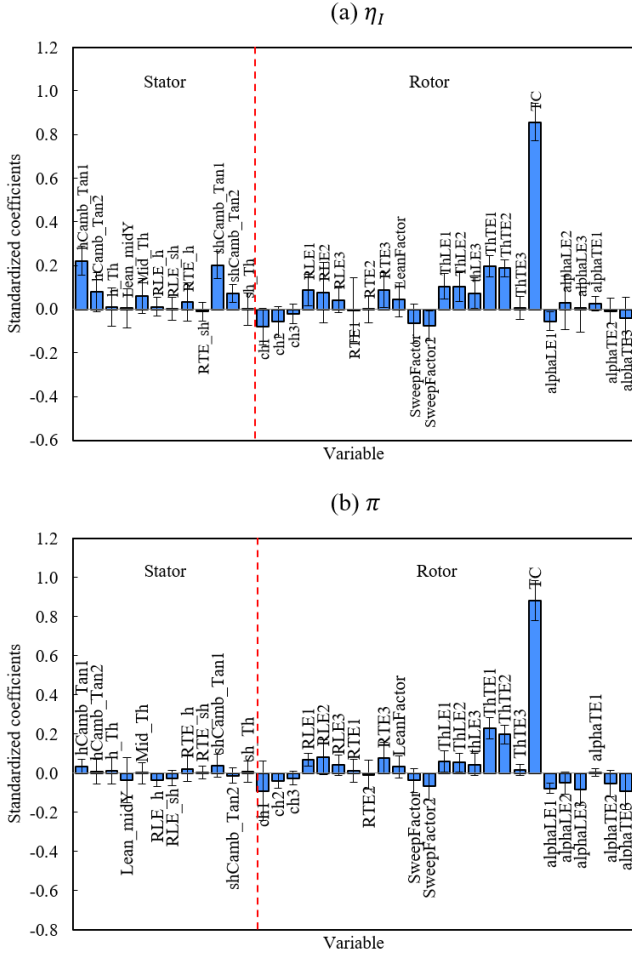


Fig.12 Bar chart showing sensitivity coefficients of (a) efficiency (b) total pressure ratio for 95% confidence interval.

To further gain some insight into design trade-offs in order to select the best designs from the robust optimization, self-organizing maps (SOM) plots [38], as presented in Fig.13, are used to distinguish the various design clusters in order to achieve the optimum trade-off zone. It's worth noting that the dataset used was only the 330 robust optimization solution. Here, the objective targets are plotted with 8 of the design variables influencing  $F_{mean}$  and  $F_{std}$ . On the far left shows the cluster zones for the objectives with red color as the highest and blue, the lowest value. The design variables are grouped into four, namely G1, G2, G3 and G4. Each zone within the neural map represents a set of design cases that follow a certain design trend and have been grouped based on the weighted values of the neurons computed during the unsupervised learning of the dataset. A total of 5 zones/design clusters were defined for this study. It was observed that zone 1 and 2 for  $F_{mean}$  and  $F_{std}$  showed the desired target of low objective values. However, zone 1 of  $F_{mean}$  showed relatively higher values compared to

that of  $F_{std}$ . This implies a negative correlation between objective targets and is evidenced in the pareto front as shown in Fig.14. For the various groups of design variables, G2 and G4 showed a positive correlation with  $F_{mean}$  and  $F_{std}$  respectively. G4 design variables were found to influence  $F_{std}$  for all design groups. Therefore, in order to achieve a better trade-off, i.e., reducing  $F_{std}$ , zone 1 of G4 will be the optimum design cases. For the other two groups, G3 showed a negative correlation with both objectives while G1 showed no correlation or a scatter, as can be said statistically. Interestingly, G1 favored a negative correlation for all objectives in zone 1 and a conflicting correlation in zone 2. Therefore, by following this design trend, it is still possible to achieve a significant reduction in  $F_{std}$  without any conflicting trade-offs. Zone 1 was therefore the best zone/cluster of design cases from which the robust optimum design was selected.

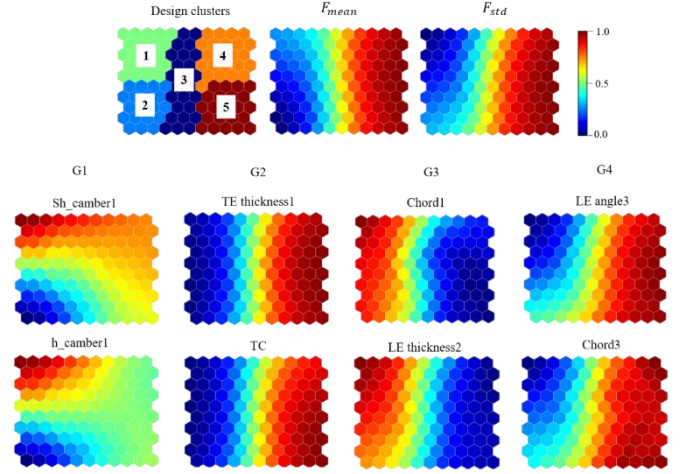


Fig. 13 Data mining of design variables against objectives.

### B. Pareto Set and Probability Distribution

Fig.14 shows the design iteration, convergence and pareto set of optimum designs for the robust optimization. The red dotted lines in the figure below shows the position of the baseline for the combined objectives  $F_{mean}$  and  $F_{std}$ . It's worth mentioning that the optimization did not fully converge since the objective target had already been met after 300 iterations and the pareto front was evident as seen in Fig.14. It is evident that  $F_{mean}$  and  $F_{std}$  are inversely related and the optimum designs are well below the baseline. Using the results from the SOM data mining, OPT 306 was selected and compared with the baseline design.

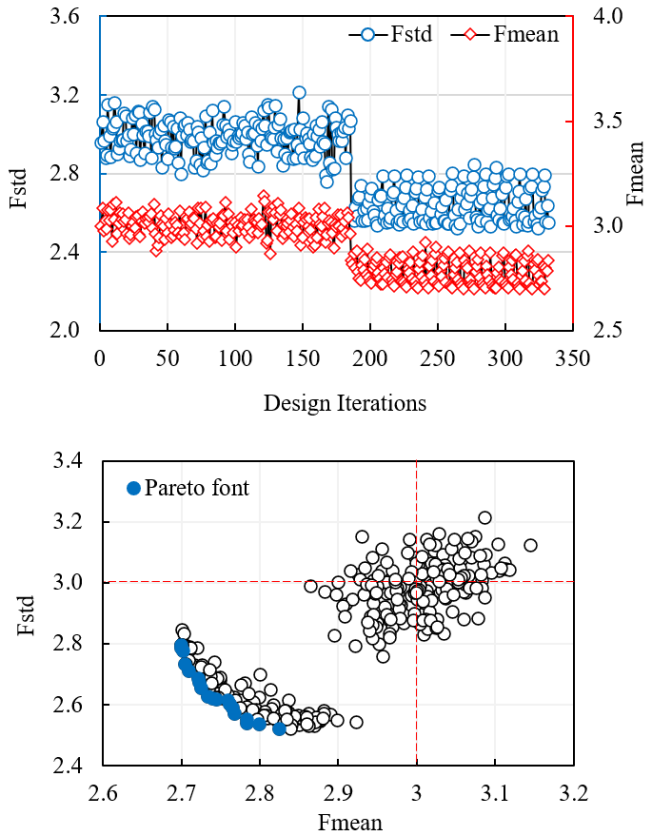


Fig. 14 Pareto set of optimum robust designs.

Fig.15 shows a comparison of the baseline design and OPT306. For the rotor, the key geometric changes observed were the chord, lean factor, thickness distribution, tip clearance and blade metal angles at the LE and TE. Significant changes were evident from 0.4 to 0.9 spanwise length. For the stator blade, mid-section thickness and lean factor were significant as seen in the figure. Furthermore, the camber tangent at the LE hub and shroud also showed significant changes compared with the baseline design. Fig 16. shows the probability density distribution of  $\eta_l$ ,  $\pi$  and  $C_p$  for the baseline and robust design at an operating condition of  $\dot{m} = 1.6 \text{ kg/s}$ . With regards to the mean performance, the mean  $\pi$  and  $\eta_l$  showed a significant reduction of 16.67% and 3.26% compared to the  $C_p$  that showed a marginal reduction of 1.98%, as shown in Table 7. All three objectives showed a reduction in standard deviation with mean  $\pi$  having the most significant reduction of 25%.

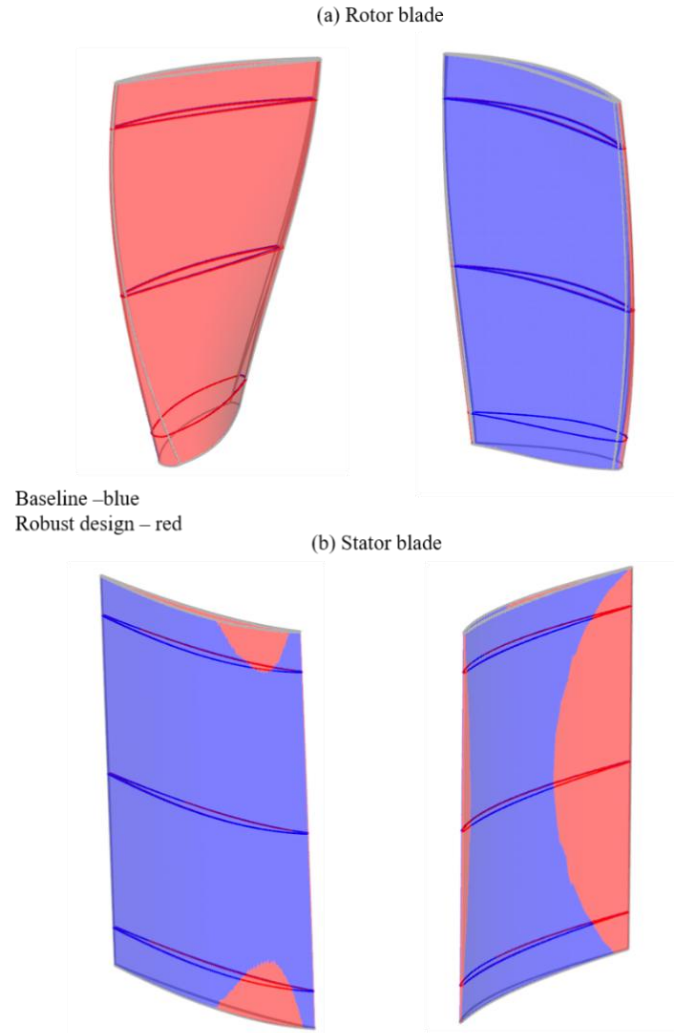


Fig. 15 Comparison of blade profiles for baseline and optimum design.

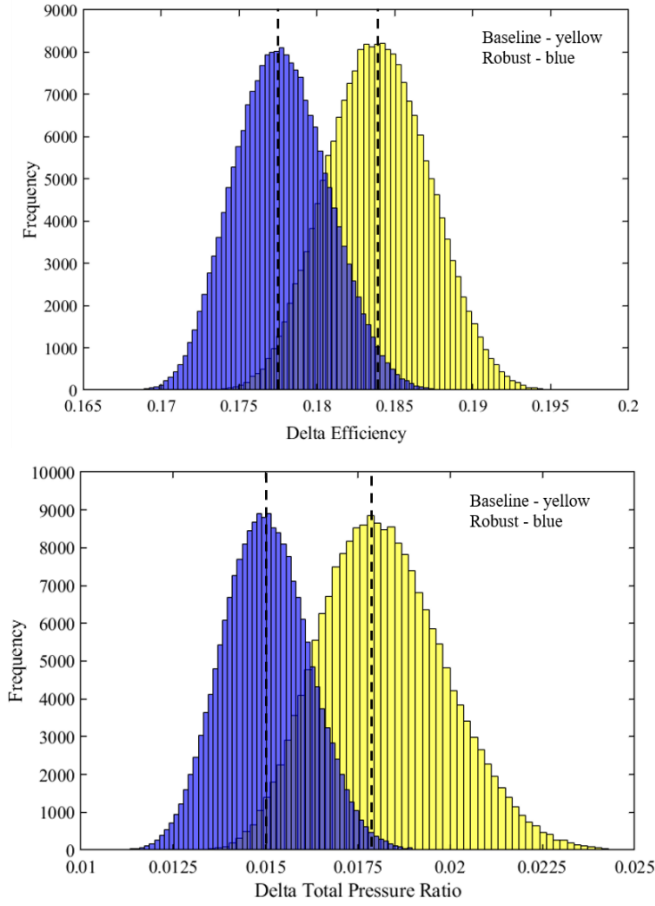


Fig. 16 Probability density distribution of objective functions for original and robust design.

### C. Stage Performance and Flow Field

Fig. 17 shows a comparison of the spanwise distribution of  $\eta_I$  and  $\pi$  for BS and RS at rotor and stage outlets. Changes in rotor efficiency were observed to be significant close to the hub from about 0.1 to 0.3 spanwise length. Only marginal changes were observed close to the tip from 0.8 span. Mid-passage had very similar distribution. A similar trend was observed at the stage exit. For  $\pi$ , improvement was observed from hub to shroud with the distribution more pronounced close to the tip for both rotor and stage performance. This is consistent with the significant increase in  $\pi$  relative to  $\eta_I$  as shown in table 7. Having identified the areas with the key changes, analysis of the flow field will focus closer to the hub and shroud.

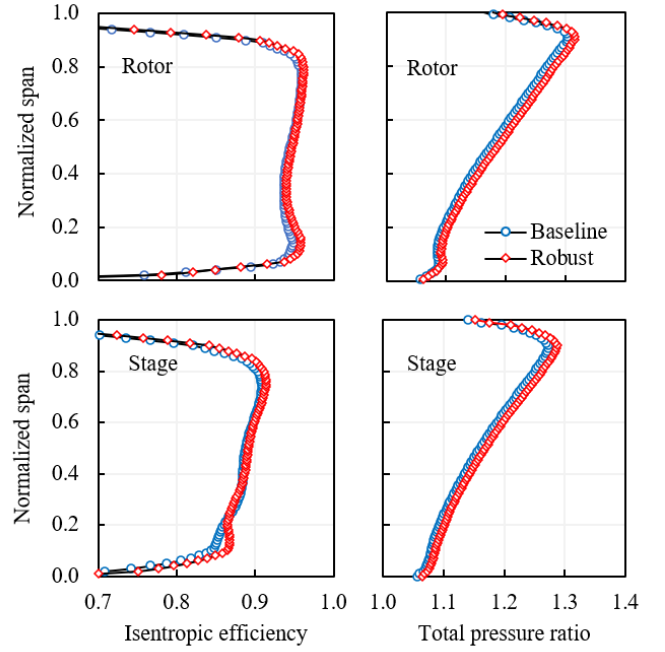
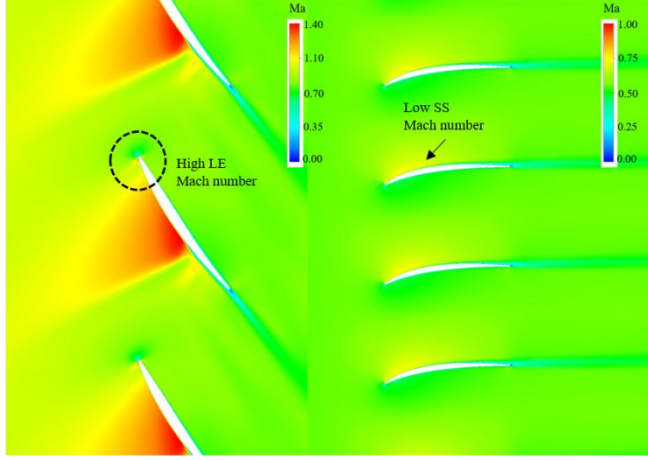


Fig. 17 Spanwise plot of isentropic efficiency and total pressure ratio at rotor and stage exit.

Fig.18 shows the relative Mach number 0.9 spanwise length for BS and RS. Although the flow distribution is similar for both designs, their magnitudes varied at the LE and TE of the rotor and the SS of the stator blade. This can be attributed to the reduction in the LE and TE radius and thickness distribution for the rotor and the increase in LE blade camber angle for the stator. This is even more evident in Fig.19 where the LE profile of the  $C_p$  value at 0.2 and 0.9 spanwise length shows significant variation for RS compared to BS. A reduction in blade loading is evident at both 0.2 and 0.9 spanwise length, which signifies a partial reduction in blockage for RS compared with BS. The change is blade aspect ratio (AR) due to the change in blade profile chord from mid-section to tip for RS influenced the blade profile losses and hence, the total loss coefficient [39, 40]. Knowing that the profile loss  $\omega_{prof}$  has a positive correlation with AR and negative with endwall loss  $\omega_{sec}$ , the increase in blade chord for constant blade height decreased the  $\omega_{prof}$ .

(a) Baseline Design



(b) Robust Design

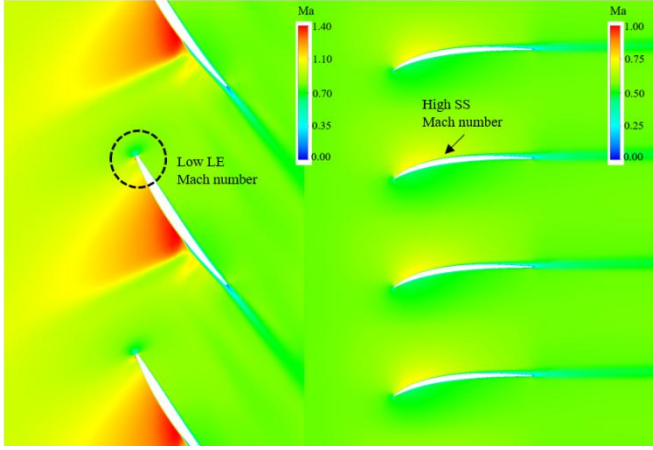


Fig. 18 Comparison of the relative Mach number distribution for BS and RS at 0.9 spanwise length.

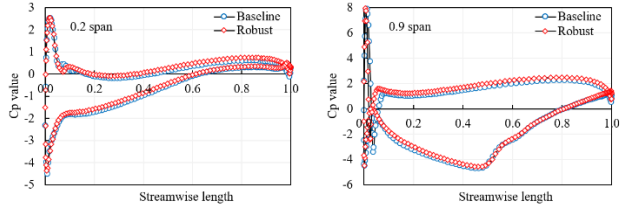


Fig. 19 Comparison of blade loading for BS and RS designs at 0.2 and 0.9 spanwise length.

Furthermore, the research work of Khalid et al [41] showed that an increase in blade solidity decreases blade loading for the same overall passage pressure rise. This reduces the leakage jet angle and the clearance mass flux resulting in a leakage jet with an effectively higher initial total pressure and hence a reduced normalized blockage. This is evident in fig.20 where there is a reduction in the low momentum fluid region, i.e., high axial velocity, for RS compared with BS. Entropy at the tip is therefore reduced. Within the blade passage, the axial flow velocity marginally decreased in magnitude close to the SS of the rotor and adjacent PS of the next blade where the velocity was highest. This was observed at 0.75 to 0.85 spanwise length. Close to the hub, changes in flow distribution were very minimal.

The resulting absolute flow angles at the rotor and stage outlets are plotted in Fig.21. RS showed an increase in flow angle from hub to shroud, with large values close to the hub, compared with BS at rotor exit. However, the stage exit of RS only changed significantly from hub to about 0.5 spanwise length. Mass averaged flow angle at stage exit was about 0.904 degrees for BS and 0.805 degrees for RS. Thus, a reduction of about 10.95%.

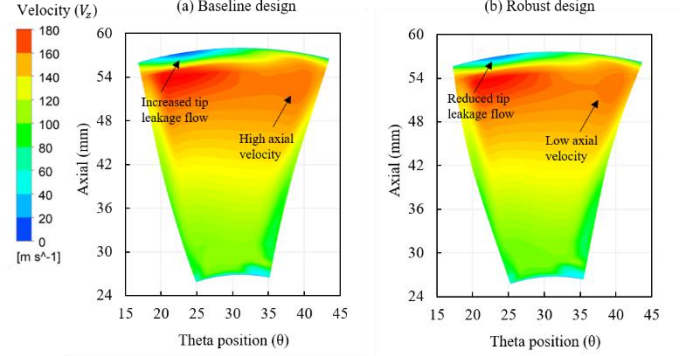


Fig. 20 Comparison of axial flow velocity distribution for BS and RS at rotor exit.

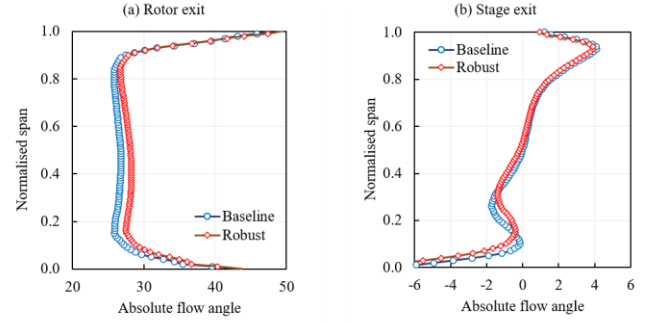


Fig. 21 Spanwise plot of absolute flow angle at rotor and stage exit.

TABLE.VII PERFORMANCE COMPARISON FOR BASELINE AND ROBUST DESIGN.

Design	$\mu_\eta$	$\mu_\pi$	$\sigma_\eta$	$\sigma_\pi$
BS	0.184	0.018	0.0032	0.0016
OPT306	0.178	0.015	0.0029	0.0012
$\Delta\%$	-3.26	-16.67	-9.38	-25.0

## V. CONCLUSIONS

In this paper, a multifidelity optimization framework for robust aero-structural design of turbomachinery blades was presented. The following conclusions can be drawn from the study.

- The proposed robust optimization strategy was able to achieve a mean aerodynamic performance comparable to the deterministic values. Efficiency, pressure ratio and pressure coefficient varied by 3.26%, 16.67% and 1.98% respectively. Reduction in deviation also varied by 9.38%, 25% and 1.35% compared with the baseline design.
- High-dimensional parameter sensitivity was explored using data mining (SOM) and observed a strong

positive correlation for LE and TE radiuses, thickness distribution and tip clearance variation against  $\eta_I$  and  $\pi$  uncertainty. The stator vane was mainly influenced by the camber distribution at the hub and shroud although the final design had a pronounced mid-section lean.

- For a given mean square error (MSE), the MFMC strategy reduced the computational cost by about 10 times for efficiency and pressure ratio and 2 times for  $C_p$  value compared with standard MC.
- The proposed strategy has established that for high-fidelity datasets that are small but highly correlated, it is possible to use only the high-fidelity CFD data combined with low-fidelity regression models. This approach has the capacity to significantly save computation time needed for complex optimization problems such as multistage multi-component problems.

## VI. ACKNOWLEDGEMENT

The authors would like to acknowledge the financial support of University of Nottingham Ningbo China (UNNC).

## VII. FUNDING

This study was fully funded by the University of Nottingham Ningbo China (UNNC) New Researchers Grant (NRG-102221200004).

## VIII. NOMENCLATURE

$D$	Diameter	[mm]
$\dot{m}$	Mass flow rate	[kg/s]
$\dot{v}$	Volumetric flow rate	[m <sup>3</sup> /s]
DoE	Design of experiments	[—]
ANN	Artificial Neural Network	[—]
LE	Leading edge	[—]
TE	Trailing edge	[—]
$\alpha$	Absolute flow angle	[—]
SS	Suction side	[—]
PS	Pressure side	[—]
NLR	Nonlinear regression	[—]
OR	Operating range	[—]
MC	Monte Carlo method	[—]
$C_p$	Pressure coefficient	[—]
PLS	Partial least squares	[—]
ANOVA	Analysis of variance	[—]
$F_\sigma$	Performance variance	[—]
$\hat{s}$	Multifidelity estimator	[—]

$e(\hat{s})$	Mean square error	[—]
$\bar{y}_{m_{i-1}}^{(i)}$	Low fidelity estimator	[—]
$Vars[\hat{s}]$	Variance	[—]
MFMC	Multifidelity Monte Carlo	[—]
$UQ$	Uncertainty quantification	[—]
$\bar{y}_{m_1}^{(1)}$	High fidelity estimator	[—]
$F_\mu$	Performance mean	[—]
$c(\hat{s})$	Multifidelity cost	[—]

## Greek Letters

$\eta_I$	Isentropic efficiency	[%]
$\pi$	Total pressure ratio	[—]
$\mu$	Mean	[—]
$\sigma$	Standard deviation	[—]
$\alpha_i$	Weighted coefficients	[—]
$\omega$	Angular velocity	[rpm]
$\xi$	Total pressure loss coefficient	[—]

## References

- [1] Kim H D, Perry A T, and Ansell P J. A Review of distributed electric propulsion concepts for air vehicle technology. In: Proceedings of AIAA/IEEE Electric Aircraft Technologies Symposium (EATS), IEEE, 2018, pp. 1-21.
- [2] Huan Z, Zhenghong G, Fang X, Yidian, Z. Review of robust aerodynamic design optimization for air vehicles,” Archives of Computational Methods in Engineering, 2019, 26(3), pp.685-732.
- [3] Orosz T, Rassölkin A, Kallaste A, Arsénio P, Pánek D, Kaska J, Karban P. Robust design optimization and emerging technologies for electrical machines: challenges and open problems. Applied Sciences, 2020, 10(19), p.6653.
- [4] Wang J, Zheng X. Review of geometric uncertainty quantification in gas turbines. ASME Journal of Engineering for Gas Turbines and Power, 2020, 142(7), p.070801.
- [5] Zhang T, Barakos G N. Review on ducted fans for compound rotorcraft. Aeronautical Journal, 2020, 124(1277), pp.941-974.
- [6] Kim J H, Kim J W, Kim K Y. Axial-flow ventilation fan design through multi-objective optimization to enhance aerodynamic performance. ASME Journal of Fluids Engineering, 2011, 133(10): 101101 (12 pages)
- [7] Fan C, Adjei R A, Wu Y, Wang A. Parametric study on the aerodynamic performance of a ducted-fan rotor using free-form method. Aerospace Science and Technology, 2020, 101, p.105842.
- [8] Zhang T, Qiao G, Smith D A, Barakos G N, Kusyumov, A. Parametric study of aerodynamic performance of equivalent ducted/un-ducted rotors. Aerospace Science and Technology, 2021, 117, p.106984.
- [9] Kamenik J, Voutchkov I, Toal D J, Keane A J, Högnér L, Meyer M, Bates R. Robust turbine blade optimization in the face of real geometric variations. Journal of Propulsion and Power, 2018, 34(6), pp.1479-1493.



- [10] Luo J, Xia Z, Liu F. Robust design optimization considering inlet flow angle variations of a turbine cascade. *Aerospace Science and Technology*, 2021, 116, p.106893.
- [11] Wang N, Yang T, Ren Z. Active subspace variation and modeling uncertainty in a supersonic flame simulation. *AIAA Journal*, 2021, 59(5), pp.1798-1807.
- [12] Wolff S. Simulation of random fields in structural design. In: Proceedings of the 11th International Probabilistic Workshop, 2013, Brno (Vol. 63, p. 66).
- [13] Peherstorfer B, Willcox K, Gunzburger M. Survey of multifidelity methods in uncertainty propagation, inference, and optimization. *Siam Review*, 2018, 60(3), pp.550-591.
- [14] Kontogiannis S G, Demange J, Savill A M, Kipouros T. A comparison study of two multifidelity methods for aerodynamic optimization. *Aerospace Science and Technology*, 2020, 97, p.105592.
- [15] Fernández-Godino M G, Park C, Kim N H, Haftka, R T. Review of multifidelity models. *ArXiv preprint arXiv:1609.07196*, 2016.
- [16] Mohammadi-Ahmar A, Mohammadi A, Raisee M. Efficient uncertainty quantification of turbine blade leading edge film cooling using bi-fidelity combination of compressed sensing and kriging. *International Journal of Heat and Mass Transfer*, 2020, 162, p.120360.
- [17] Tao J, Sun G. Application of deep learning based multi-fidelity surrogate model to robust aerodynamic design optimization. *Aerospace Science and Technology*, 2019, 92, pp.722-737.
- [18] Jabarullah Khan N K, Elsheikh A H. A machine learning based hybrid multi-fidelity multi-level Monte Carlo method for uncertainty quantification. *Frontiers in Environmental Science*, 2019, 7, p.105.
- [19] Benamara T, Breitkopf P, Lepot I, Sainvitu C, Villon P. 2017. Multifidelity POD surrogate-assisted optimization: concept and aero-design study. *Structural and Multidisciplinary Optimization*, 2017, 56(6), pp.1387-1412.
- [20] Feldmann P, Freund R. Efficient linear circuit analysis by Pade approximation via the lanczos process. *IEEE Transactions on Computer-Aided Design of Integrated Circuits and Systems*, 1995, 14, pp. 639-649, <https://doi.org/10.1109/43.384428>.
- [21] Adjei R A, Fan C, Wang W, Liu Y. Multidisciplinary design optimization for performance improvement of an axial flow fan using free-form deformation, *ASME Journal of Turbomachinery*, 2020, 143(1): 011003.
- [22] ANSYS Inc. ANSYS CFX, Release 19.2 User's Guide. ANSYS, Inc., Canonsburg, PA, 2018.
- [23] ANSYS Inc. ANSYS TurboGrid, Release 19.2 User's Guide. ANSYS, Inc., Canonsburg, PA, 2018.
- [24] Bhashyam G R, ANSYS Mechanical - A powerful nonlinear simulation tool. ANSYS Inc., USA, 1(1), 2002, p.39.
- [25] Hosder S, Grossman B, Haftka R, Mason W, Watson L, 2002. Observations on CFD simulation uncertainties. In: Proceedings of the 9th AIAA/ISSMO Symposium on Multidisciplinary Analysis and Optimization, 2002, p. 5531.
- [26] Cunnan W S, Stevens W, and Urasek D C. Design and performance of a 427 meter-per-second-tip speed two-stage fan having a 2.40 pressure ratio. NASA TP-1314, 1978.
- [27] Ursek D C, Gorrell E T, Cunnan, W S. Performance of two-stage fan having low-aspect-ratio, first-stage rotor blading. NASA TP-1493, 1979.
- [28] Liou M S, Yao W. Flutter analysis for turbomachinery using Volterra series. ASME Paper No GT2014-25474, V07BT35A004; 13 pages.
- [29] Chima R V. Viscous three-dimensional calculations of transonic fan performance. In: Proceedings of the Symposium of the Propulsion and Energetics Panel entitled CFD Techniques for Propulsion Applications, 1991, (No. NASA-TM-103800).
- [30] FRIENDSHIP SYSTEMS AG, "Product Overview", accessed September 2, 2023, <https://www.caeses.com/products/caeses/>
- [31] Peherstorfer B, Willcox K, Gunzburger M. Optimal model management for multifidelity Monte Carlo estimation. *SIAM Journal of Scientific Computing*, 2016, 38(5), pp. A3163-A3194.
- [32] Ng L, Willcox K. Multifidelity approaches for optimization under uncertainty. *International Journal for Numerical Methods in Engineering*, 2014, 100, pp. 746-772.
- [33] Adjei R A, Zheng X, Lou F, Ding C. Multifidelity optimization under uncertainty for robust design of a micro-turbofan turbine stage. *ASME Journal of Engineering for Gas Turbines and Power*, 2022, 144(10): 101006. <https://doi.org/10.1115/1.4055231>.
- [34] Marelli S, Sudret B. UQLab: A framework for uncertainty quantification in MATLAB. In: Proceedings of the 2nd International Conference on Vulnerability and Risk Analysis and Management (ICVRAM 2014), University of Liverpool, United Kingdom, 2014, pp. 2554-2563. DOI: 10.1061/9780784413609.257.
- [35] Giselle Fernández-Godino M, Park C, Kim N H, Haftka R T. Issues in deciding whether to use multifidelity surrogates. *AIAA Journal*, 2019, 57(5), pp.2039-2054.
- [36] Adams B M, Bauman L E, Bohnhoff W J, Dalbey K R, Ebeida M S, Eddy J P, Eldred M S, Hough P D, Hu K T, Jakeman J D, Stephens J A, Swiler L P, Vigil D M, Wildey T M. Dakota, A multilevel parallel object-oriented framework for design optimization, parameter estimation, uncertainty quantification, and sensitivity analysis: Version 6.0 Reference Manual," Sandia National Laboratories, Tech. Rep. SAND2014-5015.
- [37] Technical Committee ISO/TC 3. General tolerances - Part 1: Tolerances for linear and angular dimensions without individual tolerance indications. ISO 2768-1:1989.
- [38] Lemke F, Müller J A. Self-organizing data mining. *System Analysis Modelling Simulation*, 2003, 43(2), pp.231-240.
- [39] To H, Miller R J. The effect of aspect ratio on compressor performance. *ASME Journal of Turbomachinery*, 2019, 141(8): 081011. <https://doi.org/10.1115/1.4043219>.
- [40] Britsch W R. Effects of diffusion factor, aspect ratio and solidity on overall performance of 14 compressor middle stages. NASA Technical Paper 1523, NASA Lewis Research Center Cleveland, OH, United States, 1979.
- [41] Adamczyk J J, Celestina M L, Greitzer E M. The role of tip clearance in high-speed fan stall. *ASME Journal of Turbomachinery*, 1993, 115(1), pp.28-38.

## Authors' background

<b>Name</b>	<b>Prefix</b>	<b>Research Field</b>	<b>Email</b>	<b>Personal website</b>
Richard Amankwa Adjei	Assistant Professor	Fluid machinery, Electric propulsion system	Richard-Amankwa.Adjei@nottingham.edu.cn	
Salman Ijaz	Assistant Professor	Control systems of more electric aircraft	salman.ijaz@nottingham.edu.cn	
Junyuan Jiang	Undergraduate Student	Fluid machinery, Electric propulsion system	ssyjj1@nottingham.edu.cn	
Yiwei Wang	Undergraduate Student	Fluid machinery, Electric propulsion system	ssyyw13@nottingham.edu.cn	